Research Square

Preprints are preliminary reports that have not undergone peer review.
They should not be considered conclusive, used to inform clinical practice,
or referenced by the media as validated information.

Conformational Entropy Bottleneck Underlies Nanopore Interception of Polymers: Dominant Roles of Branching Architecture and Excluded Volume

Lianwei Li

lianweili@szu.edu.cn

Shenzhen University

Yiren Wang

Shenzhen University

Haorong Huang

Shenzhen University

Jiawen Yang

Guangdong University of Technology

Xin Guan

Shenzhen University

Mo Zhu

Shenzhen University

Mingming Ding

Guangdong University of Technology

Article

Keywords:

Posted Date: February 19th, 2026

DOI: https://doi.org/10.21203/rs.3.rs-8805080/v1

License: This work is licensed under a Creative Commons Attribution 4.0 International License.
Read Full License

Additional Declarations: There is **NO** Competing Interest.

Version of Record: A version of this preprint was published at Nature Communications on September 29th, 2026. See the published version at https://doi.org/10.1038/s41467-026-78055-1.

Conformational Entropy Bottleneck Underlies Nanopore Interception of Polymers: Dominant Roles of Branching Architecture and Excluded Volume

Yiren Wang[1], Haorong Huang[1], Jiawen Yang[2], Xin Guan[1], Mo Zhu[1], Mingming Ding[2], Lianwei Li[1*]
[1] *College of Chemistry and Environmental Engineering, Shenzhen University, Shenzhen, China 518060*
[2] *School of Chemical Engineering and Light Industry, Guangdong University of Technology, Guangzhou, China 510006*

Abstract: The transport of polymers through nanopores is fundamentally governed by the interplay between molecular topology and nanoconfinement. However, how branching architecture influences the critical interception size ($R_{h,c}$) under weak compression—where diffusion dominates and chain deformation is negligible—remains poorly understood. Here, we address this challenge by integrating well-defined hyperbranched polystyrenes with tunable branch densities (ρ = 1/25-1/650) monodisperse anodic aluminum oxide nanopores (D = 28-96 nm), all-atom simulations, and theoretical modeling to uncover a conformational entropy bottleneck mechanism. We experimentally reveal a distinct power-law relationship $R_{h,c} \sim \rho^{-1/2}$ for hyperbranched polymers, in stark contrast to the classic behavior of linear chains. Moreover, hyperbranched architectures exhibit markedly weaker temperature dependence in interception behavior, attributed to enhanced intrachain excluded volume interactions. A combination of molecular dynamics simulation and theoretical analysis confirms that branching restricts conformational fluctuations, narrowing the distribution of accessible states and raising the free-energy barrier for pore entry. Our findings establish branching topology as a key regulator of polymer transport and interception in nanopores, offering new insights into the behavior of biopolymers like glycogen and starch in confined environments and guiding the design of advanced separation systems.

*To whom correspondence should be addressed: lianweili@szu.edu.cn

Introduction

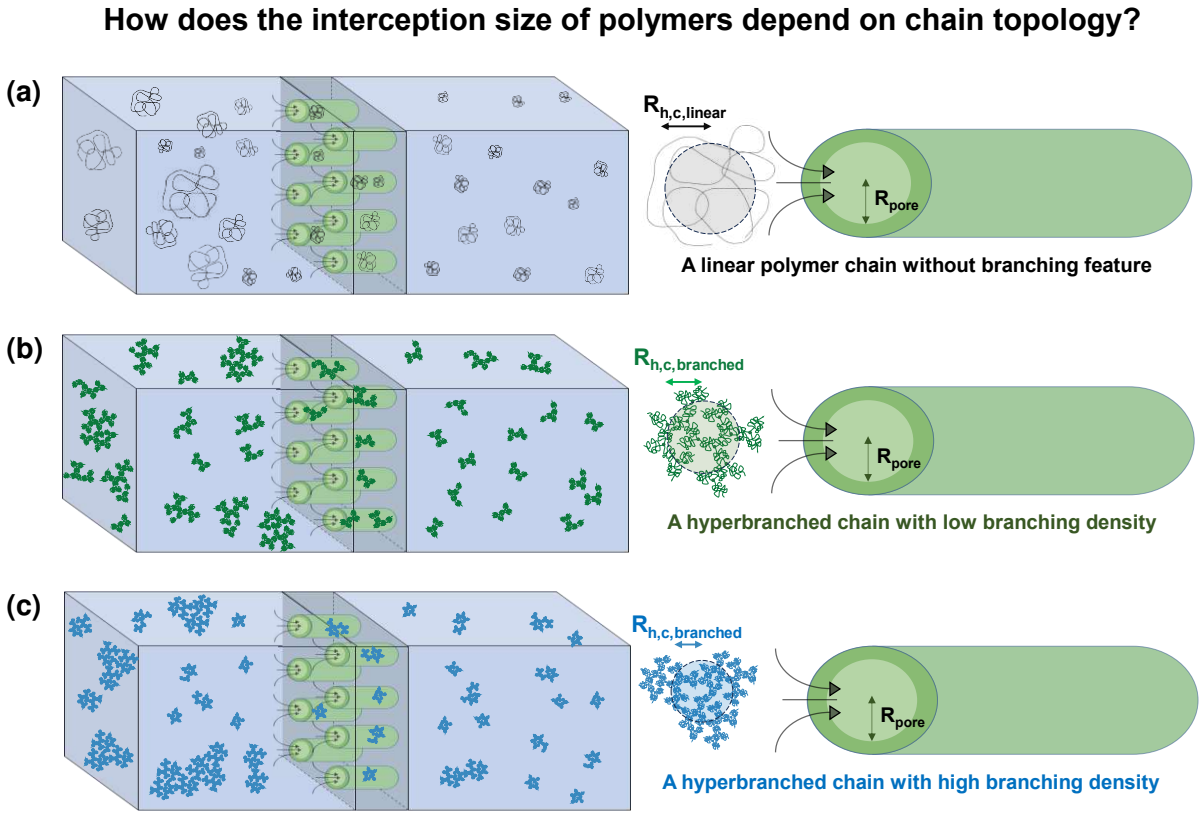
The transport and diffusion of macromolecules in nanoconfined porous media underpin key physicochemical processes in biological membranes (e.g., glomerular filtration[1], RNA transport[2], protein translocation[3, 4]) and advanced separation technologies (e.g., gene sequencing[5], nanosensing[6], water treatment[7]). These phenomena critically rely on the interplay between molecular topology—ranging from linear and cyclic to globular and hyperbranched architectures—and nanoscale confinement. Based on local flow intensity, confined polymer transport bifurcates into two distinct regimes: the strong-compression limit, where high-velocity flow induces substantial chain deformation (e.g., coil-to-globule transition)[8], and the weak-compression limit, governed by ultra-low flows where diffusion dominates[9]. Although theoretical frameworks, including confined blob models[10-12], free energy analyses[13], and mechanical descriptions[14] have extensively elucidated strong-compression dynamics—characterized by entropic elasticity, viscous dissipation, and topological disentanglement—for diverse architectures such as linear, star, comb, hyperbranched polymers, and microgels[15-18], the weak-compression limit remains poorly understood and a subject of ongoing debate.

The weak-compression limit, serving as the physical foundation of transport phenomena and being directly relevant to biological filtration, is characterized by near-equilibrium conditions, negligible deformation, diffusion-dominated dynamics, and a critical interception event when polymer dimensions approach the pore size[19]. The corresponding critical interception size ($R_{h,c}$) represents an essential entropic bottleneck for molecular transport. Understanding the determinants of $R_{h,c}$—particularly how molecular topology (especially branching) governs the critical conformational size under weak compression—constitutes a frontier challenge in soft matter science. Although previous studies under equilibrium conditions have established that

the interception behavior of linear polymers is universal and independent of chemical composition[20], these conclusions are largely based on architectures with linear connectivity (e.g., linear and star polymers), which fail to predict the behavior of highly branched systems like glycogen or starch[21, 22]. This gap raises a fundamental question: Is $R_{h,c}$ universal across polymers with vastly different topologies, such as linear and hyperbranched chains, in identical nanoconfined environments?

Indeed, recent studies on hyperbranched and other highly branched polymers have revealed that these systems exhibit complex multi-body hydrodynamic interactions, where the two-body approximation often fails. These interactions alter key scaling relationships—such as size-to-mass scaling and rheology—distinguishing them sharply from linear chains.[23, 24] For instance, hyperbranched polystyrenes with uniform subchains show a unique double dependence in the Mark-Houwink-Sakurada relationship, i.e., $[\eta]\sim M_{total}^{0.39} M_{sub}^{0.31}$, reflecting their compact architecture and reduced hydrodynamic volume[25]. In contrast, perfectly symmetric dendrimers lack fractal characteristics—a qualitative departure resulting from their ideal, defect-free, and overcrowded branching structure[26].

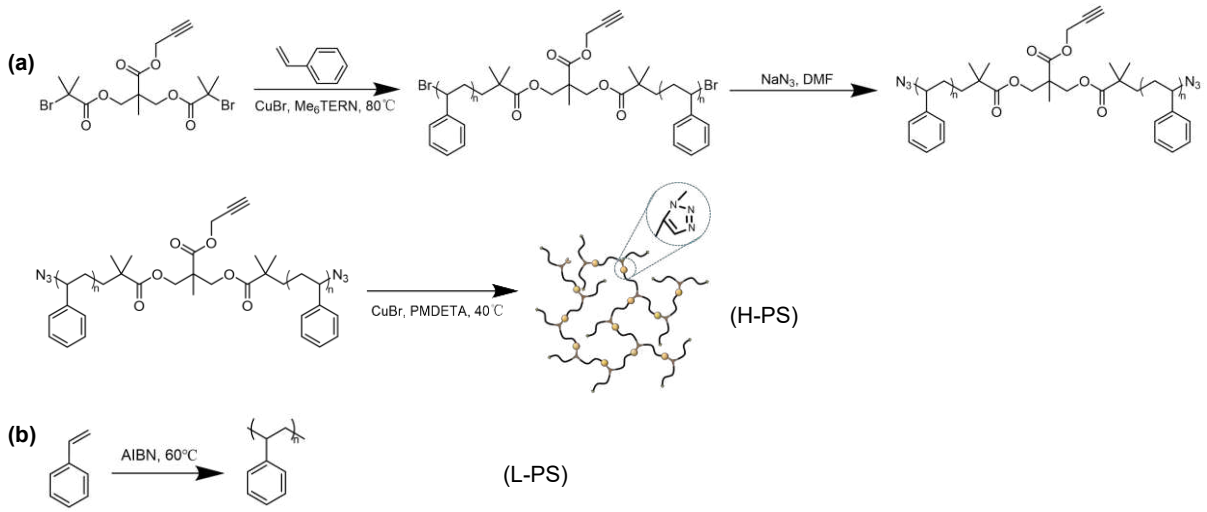
We therefore hypothesize that hyperbranched polymers should exhibit distinct interception behavior from linear chains, namely, $R_{h,c}$ may depend on the branching architecture. This distinction may originate from their highly branched topology, which promotes compact, globular conformations with restricted fluctuations, while simultaneously amplifying the excluded volume effect and enhancing chain rigidity. To address this hypothesis, it require well-defined model systems: nanopores with controlled geometry, strictly regulated ultra-low flows, and topologically standardized polymers with precise branching parameters.



Scheme 1. Polymer translocation and interception through nanopores depends on branching topology under strictly controlled ultra-low flows. (a-c) Schematic illustration of linear (L-PS) and hyperbranched (H-PS) polystyrene chains with varying branching densities diffusing through cylindrical nanochannels under weak compression limit and ultra-low flow, where $R_{h,c}$ and R_{pore} denote the critical interception size and nanopore radius, respectively.

To test our hypothesis (**Scheme 1**), we employed a model-decoupling strategy combining custom anodic aluminum oxide (AAO) nanopore arrays with controlled geometry and well-defined hyperbranched polystyrene (H-PS) samples of tuned branching density (ρ), alongside linear PS (L-PS), under strictly controlled ultra-low flows. Key results reveal: (1) For pores (28-96 nm), increasing ρ from 1.54×10^{-3} to 4.00×10^{-2} reduces the critical hydrodynamic interception size ($R_{h,c}$) with scaling $R_{h,c} \sim \rho^{-1/2}$, significantly below L-PS values; (2) Theoretical analysis and all-atom simulation confirm that branching governs conformational fluctuations, free energy barriers, and translocation probability; (3) While the increase in temperature expands the chain dimensions, $R_{h,c}$ remains nearly constant for hyperbranched architectures—

unlike the strong temperature dependence in linear chains—demonstrating topology-dominated exclusion effects under weak compression.



Scheme 2. Synthetic routes to architecturally-defined polystyrene samples for nanopore interception studies. (a) Hyperbranched polystyrene (H-PS) with controlled branching densities synthesized via integrated ATRP and CuAAC 'click' chemistry, ensuring uniform subchains and broad molecular weight distribution. (b) Linear polystyrene (L-PS) prepared by conventional AIBN-initiated free radical polymerization, providing broad-distribution samples for comparative studies.

Results and Discussion

Sample Preparation and Structural Characterization. **Scheme 2** outlines the synthetic routes for model hyperbranched (H-PS) and linear (L-PS) polystyrene samples. H-PS architectures were synthesized via a group-developed strategy combining atom transfer radical polymerization (ATRP) and copper-catalyzed azide-alkyne cycloaddition (CuAAC) click chemistry[27-29]. Using well-characterized AB_2-type macromonomers with degrees of polymerization (DP) ranging from 50 to 1300 (**Figures S1-S3**), we obtained hyperbranched structures possessing branch lengths of 25-650 styrene units, corresponding to branching densities (ρ) from 1/25 to 1/650. For each macromonomer, a series of H-PS samples (denoted H-PS_ρ) were prepared, covering an apparent weight-average molecular weight ($M_{w,app}$) range of 0.19×10^5-5.13×10^5 Da and polydispersity indices (Đ) of 1.51-6.89 (**Table S1**). The subchain

segments of H-PS_ρ samples exhibit flexible characteristics, given that the Kuhn length of PS is approximately 1.5 nm (≈ 7 styrene units)[30, 31]. In parallel, L-PS samples were prepared via conventional AIBN-based free-radical polymerization, yielding materials with $M_{w,app}$ = 0.96×10^5-9.8×10^5 Da and Đ = 2.12-2.89 (**Table S2**).

Unlike previous studies that relied on sporadic, discrete samples to estimate pore-passage probability or identify a critical interception size, such a sparse sampling strategy inherently increases experimental uncertainty, making it difficult to precisely pinpoint the true critical size for diffusion through a pore[32-34]. In contrast, our use of broadly distributed samples enables a continuous assessment of interception probability as a function of chain length or molecular weight, thereby avoiding the ambiguities associated with selectively chosen discrete data points. Although SEC provides only an apparent molecular weight for non-linear architectures, it affords reliable hydrodynamic size estimations. Grounded in the universal principle of size exclusion, SEC served as the most suitable method for resolving the continuous, broad molecular weight distributions essential for this study.

The raw SEC chromatograms (**Figures 1a-e**) were calibrated using linear polystyrene standards to establish a definitive M versus $V_{retention}$ relationship (**Figure S4**). Applying universal scaling laws for hydrodynamic radius R_h and gyration radius R_g versus M (**Figure S5**), we transformed these into continuous profiles of R_h (**Figures 1f-j**) and $R_{g,app}$ (**Figures 1k-o**). R_h closely approximates the true hydrodynamic radius for hyperbranched samples, whereas $R_{g,app}$, derived from linear chains, may deviate from actual R_g due to architectural differences and serves as a reference. Quantitatively, the hydrodynamic diameters ($2R_h$) for samples (L-PS, H-$PS_{1/650}$, H-$PS_{1/170}$, H-$PS_{1/95}$, H-$PS_{1/25}$) span ~10 to ~100 nm, with some extending sub-10 nm

or exceeding 100 nm, providing a solid foundation for systematically probing interception behavior across pore sizes.

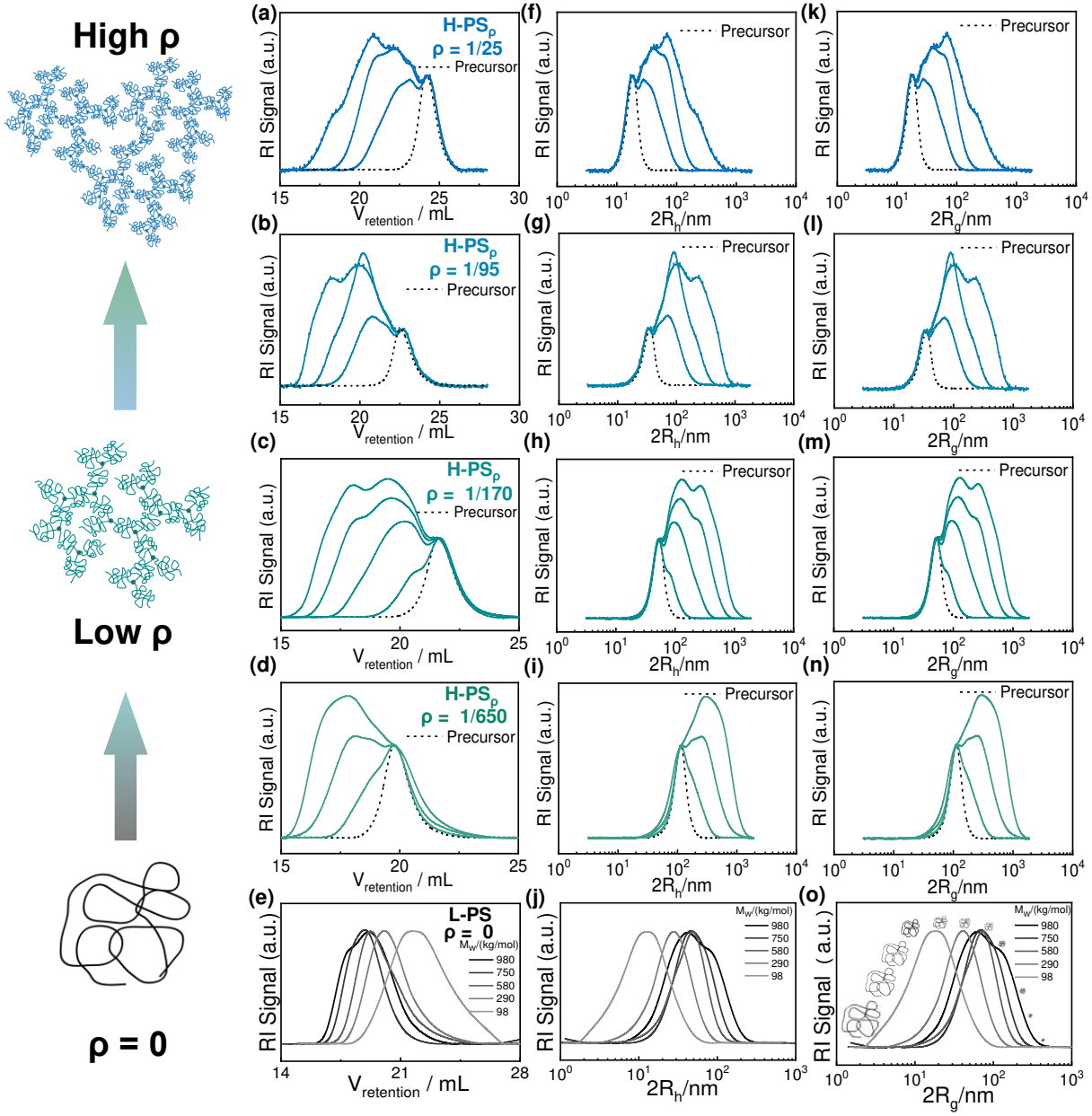


Figure 1. Hydrodynamic interception size characterization of linear and hyperbranched polystyrene samples. (a-e) SEC raw curves for L-PS and H-PS samples with varying branching densities (ρ) and molecular weights (M). (f-j) Hydrodynamic diameter ($2R_h$) profiles derived from SEC calibration, where the broad hydrodynamic size distribution (~10-100 nm) enables systematic interrogation of interception behavior across nanopores of different diameters. (k-o) Apparent radius of gyration ($R_{g,app}$) profiles.

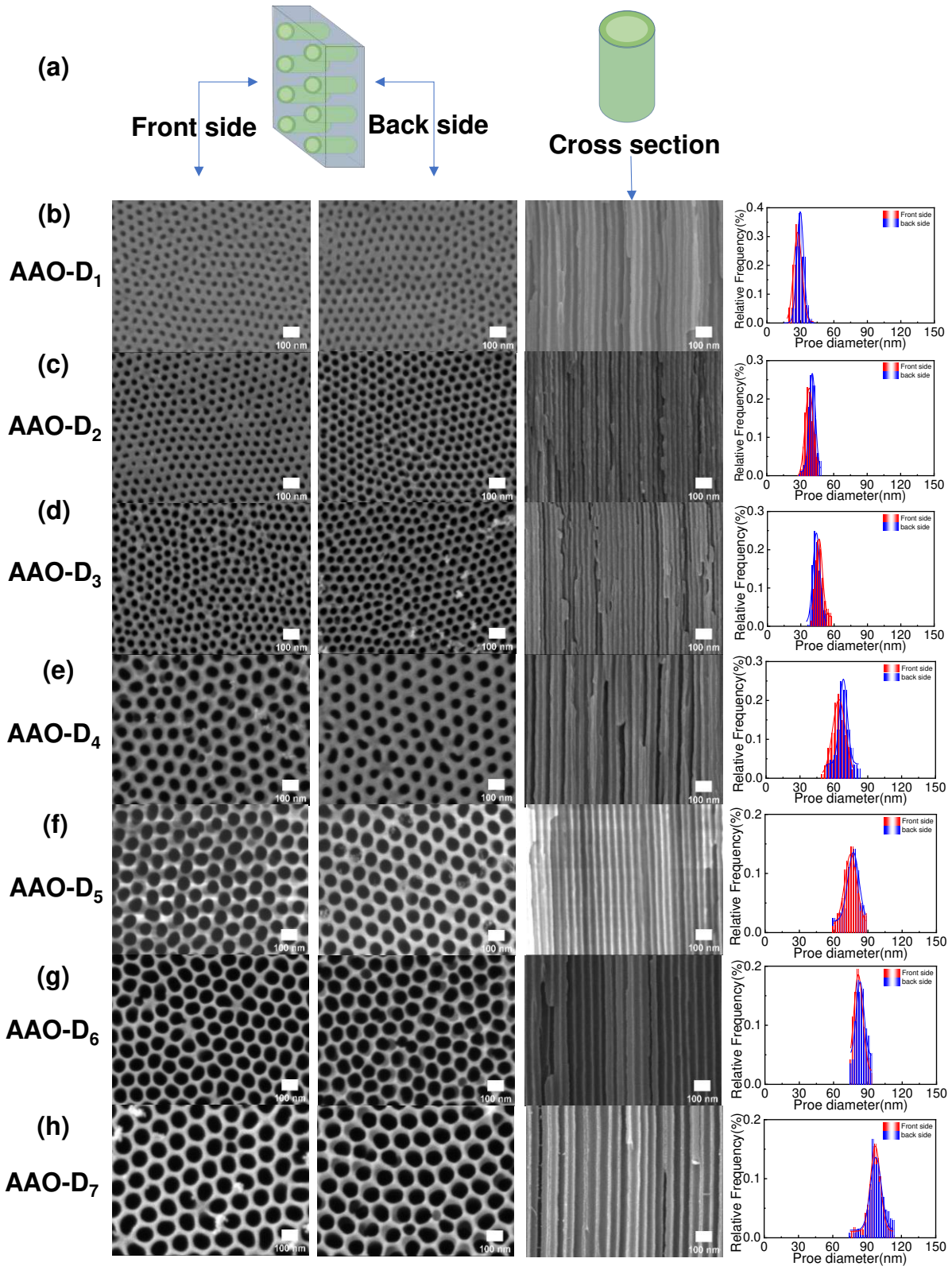


Figure 2. Structural uniformity of anodic aluminum oxide (AAO) nanopores enables precise interception studies. (a) Schematic illustration of Top-surface, bottom-surface, and cross-section of AAO nanopore. (b–h) SEM images of for AAO-D_1 to AAO-D_7 cylindrical pore morphology, with mean diameters ranging from ~28 to 96 nm and polydispersity indices (Đ) < 1.02, demonstrating well-defined and high geometric uniformity, where the insets show pore size distribution histograms corresponding distribution curves.

Nanopore Uniformity and Interception Protocol Validation. The availability of well-defined nanoporous membranes is crucial for reliable interception studies. Based the previous work[35, 36], we fabricated a batch of anodic aluminum oxide (AAO-D_n) nanochannel membranes. These membranes exhibit average pore diameters (D) ranging from ~28 to ~96 nm (AAO-D_1 to AAO-D_7), a consistent channel length of ~50 μm, and a pore density of approximately 6.2×10^9 to 2.7×10^{10} pores/cm^2 (**Table S3**), providing the basis for estimating single-pore diffusion and microscopic flow rates. Structural characterization confirmed the high quality of the AAO-D_n membranes (**Figure 2a**). Statistical analysis of the pore size distributions (**Figures 2b-h**) revealed nearly circular pores on both top and bottom surfaces, with mean diameters differing by < 2.0 nm and a narrow polydispersity index (Đ < 1.02). Cross-sectional imaging further verified their well-defined, parallel cylindrical morphology, establishing the AAO-D_n series as quasi-ideal model porous media for interception experiments.

In addition to SEM characterization, we employed a transmembrane pressure method to assess the average pore size of the AAO-D_n membranes (**Figure S6**). Sequential filtration experiments were performed using pure solvent followed by PS samples of varying topologies (L-PS and H-PS with different ρ). Filtrates from each interception step were analyzed by SEC to determine the critical hydrodynamic interception size.

Figure 3a depicts a sequential interception experiment conducted in the order: linear L-PS → low-branching-density H-PS → medium-branching-density H-PS → high-branching-density H-PS → linear L-PS. Following each interception, a reverse solvent flush was employed to mitigate concentration polarization and membrane contamination, while the transmembrane pressure difference (ΔP) was monitored at each step. Initial ΔP after L-PS interception using a D = 32 nm AAO membrane was 117 kPa, with subsequent values of 114, 122, 123, and 124

kPa. The minimal pressure variation indicates membrane stability, corroborated by similar results for a D = 72 nm membrane (**Figure S7**).

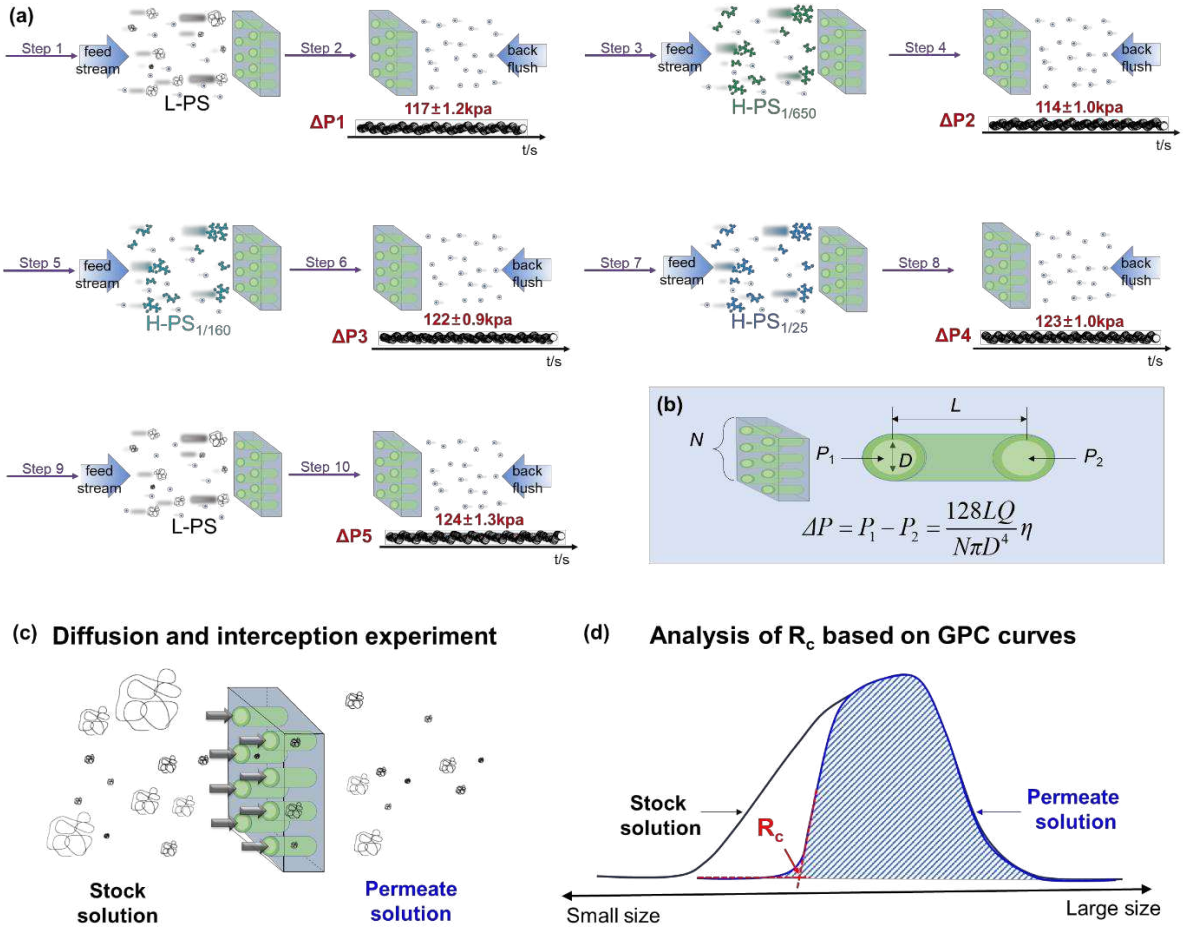


Figure 3. Sequence interception experiments and transmembrane pressure measurements. (a) Sequential interception protocol (L-PS → low-ρ H-PS → medium-ρ H-PS → high-ρ H-PS → L-PS) with reverse solvent flushing to minimize polarization effects, where transmembrane pressure (ΔP) remains stable (117-124 kPa) during experiments with D = 32 nm AAO membranes, indicating structural integrity. (b) Poiseuille equation-based analysis correlating pore diameter (D), channel length (L), pore density (n), solvent viscosity (η), and flow rate (Q). (c) Schematic diagram of diffusion and cutoff experiment. (d) The retention size is obtained based on the molecular information of the original solution and the permeate solution through chromatographic analysis.

The transmembrane pressure (ΔP) correlates with pore diameter (D), channel length (L), pore density (n), solvent viscosity (η), and flow rate (Q) via the Poiseuille equation (**Figure 3b**). Since $\Delta P \sim 1/D^4$, the slight increase from 117 kPa to 124 kPa corresponds to a negligible pore diameter change (~1.5%), confirming the structural integrity and uniformity of the AAO membranes. Control experiments further validated the Poiseuille equation's applicability,

showing linear relationships for both variable pore diameters (fixed solvent) and variable solvents (fixed pore), as summarized in **Figure S8**. Excellent agreement between pore sizes derived from the Poiseuille equation and SEM analysis (**Table S3**) reinforces the robustness of this hydrodynamic approach for assessing membrane permeability and pore stability.

Interception experiments were conducted at Q = 0.2 mL/h with temperature maintained at 25 ± 1 °C and polymer concentration below 1.00 g/L. Approximately 10 mL of pre-filtered polymer solution is injected into the syringe. Quantitatively, the microscopic flow rate (q) for each single pore was calculated to be $q = 2.06\times10^{-21}$ ~ to 8.97×10^{-21} m^3/s based on the pore density data (6.20×10^9 to 2.71×10^{10} pores/cm^2), corresponding to the microscopic flow velocity of ~1.24×10^{-6} to 3.35×10^{-6} m/s (**Table S3**), which is 10~10^2 times smaller than that of solvent molecules. The provided flow disturbance is much smaller than the fluctuation of solvent motion excited by thermal energy, which can ensure that the designed system belongs to the weak compression limit. In addition, the cumulative hydrodynamic shear energy acting on a molecule (with an estimated contour length of 50-1000 nm) is ~1.9×10^{-6} to 7.9×10^{-6} k_BT, significantly lower than the thermal energy k_BT.

Branching-Dependent Interception Behavior. It is worth noting that for the four samples to be intercepted, we all followed the principle of selecting samples from the sample library that are slightly larger in size than the pore diameter, in order to weaken the concentration difference and polarization effects. Taking the hyperbranched sample with ρ = 1/650 as an example, since the pore diameters of D_1-D_3 are small, we chose the sample with a smaller molecular weight (**Table S1**, **entry 11**), while the corresponding D_4-D_7 were selected from samples with a larger molecular weight (**Table S1**, **entry 12**). **Figures 4a-g** presents the raw SEC data from sequential interception experiments for linear and hyperbranched polymers across nanopores

with diameters ranging from 28 to 96 nm. Consistently, branching-dependent interception curves were observed across all pore sizes. For example, in the case of pore D_6 (88 nm), the critical retention volume ($V_{r,c}$) increased sequentially with increasing branching density: $V_{r,c}$ values for H-$PS_{1/650}$, H-$PS_{1/170}$, and H-$PS_{1/95}$ were measured as 16.82 mL, 17.16 mL, and 17.42 mL, respectively.

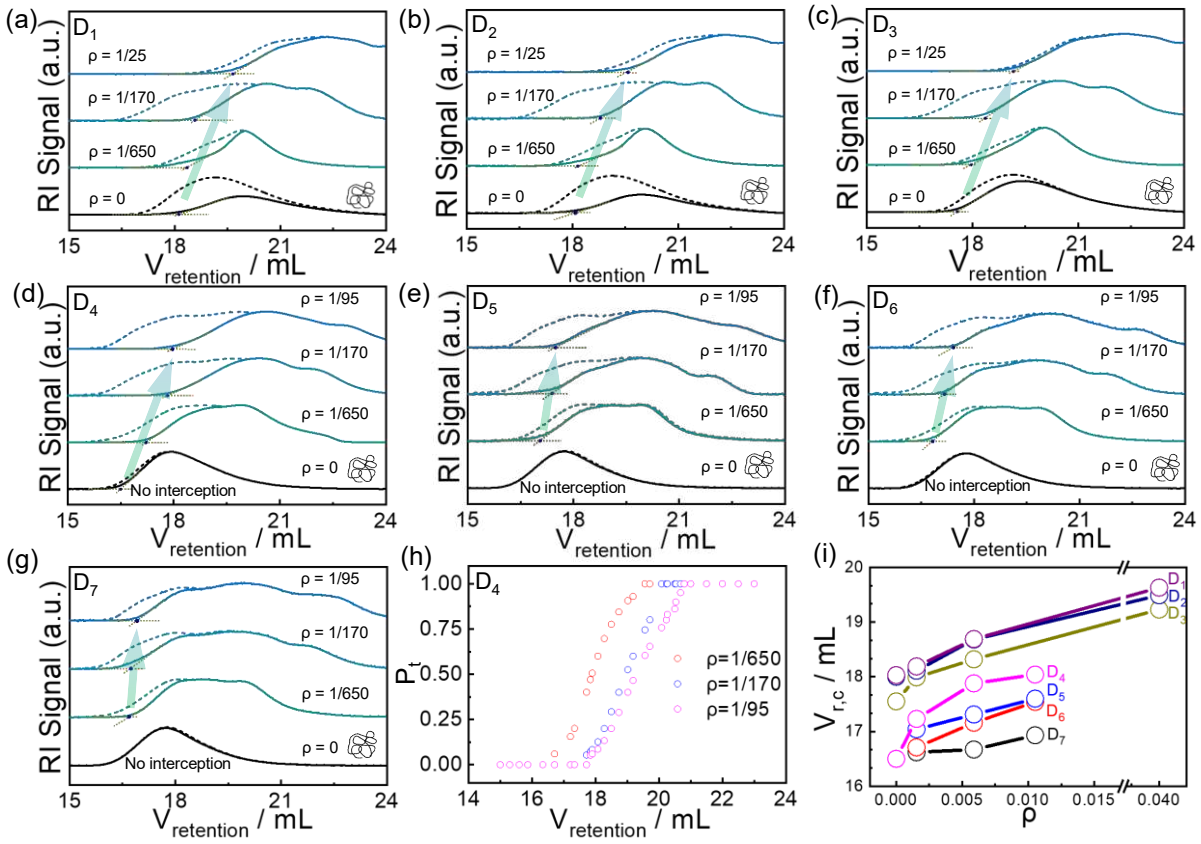


Figure 4. Branching-dependent interception behavior for L-PS and H-PS samples across nanopores with different diameters. (a–g) SEC curves (retention volume vs. RI signal) of feed and permeate solutions for linear L-PS (ρ = 0) and hyperbranched polystyrenes (H-PS) with increasing branching density (ρ, bottom to top) and, using AAO membranes with pore diameters D_1–D_7 (28-96 nm), where experiments were conducted at T = 25°C, Q = 0.20 mL/h, and below C = 1.00 g/L. (h) Dependence of translocation probability (P_t) on critical retention volume ($V_{r,c}$) for nanopore D_4 = 55 nm. (i) Dependence of critical retention volume $V_{r,c}$ on ρ for different nanopore sizes.

Linear PS exhibited distinct pore-size-dependent interception: no significant interception was detected for pores larger than 55 nm (e.g., D_4), indicating that even the largest chains in the broad-distribution sample could pass through. In contrast, for pores smaller than 55 nm, a clear critical retention volume emerged. This finding is intriguing given that SEC analysis indicated

a maximum hydrodynamic diameter of ~100 nm for L-PS, suggesting a discrepancy that can be rationalized by the inherent band-broadening effects in SEC, which distort size estimation for species at the distribution extremes. For hyperbranched PS, although some samples had sizes comparable to the pore dimensions, extensive statistical analysis unequivocally demonstrated that the interception size is primarily governed by branching density, with higher density leading to a smaller critical interception size.

Beyond the analysis of critical interception sizes (**Figures 4a-g**), the translocation probability as a function of retention volume, $P_t(V_r)$, offers a comprehensive perspective over the full chain-length distribution. **Figure 4h** shows the pore-passage probability versus retention volume for all samples tested with the D_4 pore, demonstrating a gradual transition from 100% interception at large sizes to 100% diffusion passage at small sizes. $P_t(V_r)$ curves for other pore sizes are provided in **Figure S9**.

The critical interception size, $R_{h,c}$, for each polymer-pore combination was objectively determined from these $P_t(V_r)$ curves. Taking into account the broadening effect of the SEC curve, we define $R_{h,c}$ as the hydrodynamic radius at which the interception starts. The critical $V_{r,c}$ can be converted to $R_{h,c}$ using the well-established SEC calibration relationship between retention volume and hydrodynamic radius (**Figures S4** and **S5**).The use of broadly distributed polymer samples was crucial here, as it enabled a continuous mapping of P_t versus R_h, thereby avoiding the ambiguities associated with interpreting data fromonly a few discrete molecular weights. Representative examples illustrating the determination of $V_{r,c}$ from the interception probability curves are provided in **Figure S10**.

A key observation is that linear chains display a broader transition interval in retention volume—from full interception to full passage—than hyperbranched chains. This wider

transition window, corresponding to an extended size range, is intrinsically associated with the broader conformational fluctuations typical of linear chains. These results clearly demonstrate that branching density systematically shifts the interception curves, suggesting a topology-dependent critical size. To quantify this dependence, we next perform a scaling analysis to extract $R_{h,c}$ as a function of ρ.

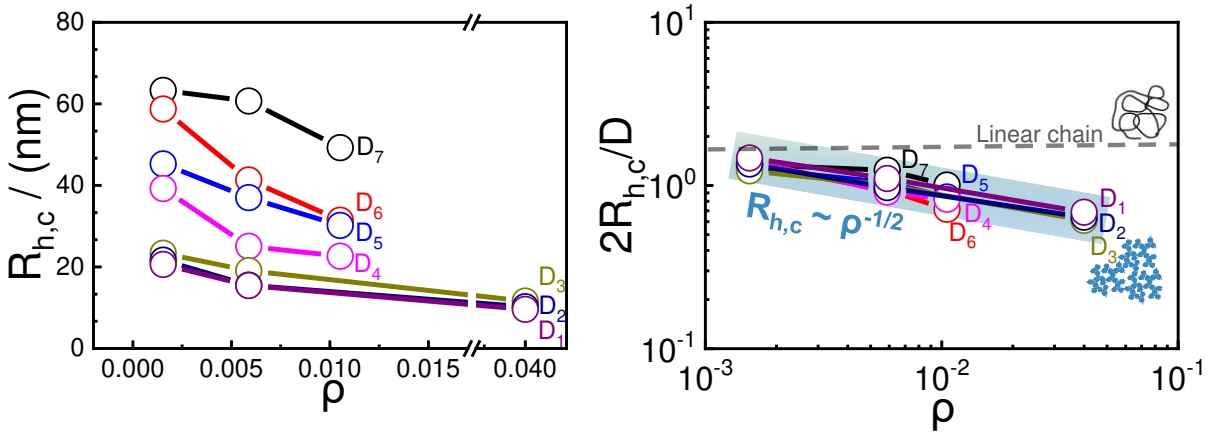


Figure 5. Dependence of critical interception hydrodynamic radius on branching density. (a) Critical interception hydrodynamic radius ($R_{h,c}$) versus branching density (ρ) for AAO nanopores with diameters D_1-D_7 (28-96 nm), where $R_{h,c}$ decreases systematically with increasing ρ across all pore sizes. (b) Normalized scaling relationship ($2R_{h,c}/D$ versus ρ) on logarithmic axes, where all data collapse into a master region described by $R_{h,c} \sim \rho^{-1/2}$ (roughly described by the blue band), confirming the topology-driven control of nanopore interception.

Scaling Analysis of Critical Interception Size. Building on the interception profiles presented in **Figure 4**, we now systematically extract the critical hydrodynamic interception size $R_{h,c}$ for each branching density and pore size. **Figure 5a** presents absolute $R_{h,c}$ values, while **Figure 5b** shows the pore-diameter-normalized quantity $2R_{h,c}/D$. As shown in **Figure 5a**, a universal trend emerges across all pore sizes (D_1-D_7): $R_{h,c}$ decreases systematically with increasing ρ. For example, with pore D_3 (41 nm), $R_{h,c}$ drops from ~27 nm for linear PS (ρ = 0) to ~15 nm for highly branched H-$PS_{1/25}$ (ρ ≈ 0.04), confirming the strong dependence of interception size on molecular topology. The normalized analysis in **Figure 5b** offers deeper physical insight. The double-logarithmic plot can be roughly described by the blue band with a power-law scaling of

$2R_{h,c}/D \sim \rho^{-1/2}$,, which starkly contrasts with the behavior of linear chains and points to a distinct entropic bottleneck mechanism. This revealed scaling analysis, *for the first time*, displays how molecular topology governs interception under nanoconfinement—specifically, increased branching density yields more compact architectures, reducing the effective size required for nanopore passage. We further hypothesize that the dependence of $2R_{h,c}/D \sim \rho^{-1/2}$ should be attributed to the difference in conformational distribution and the free energy barrier for pore translocation when compared with linear chains.

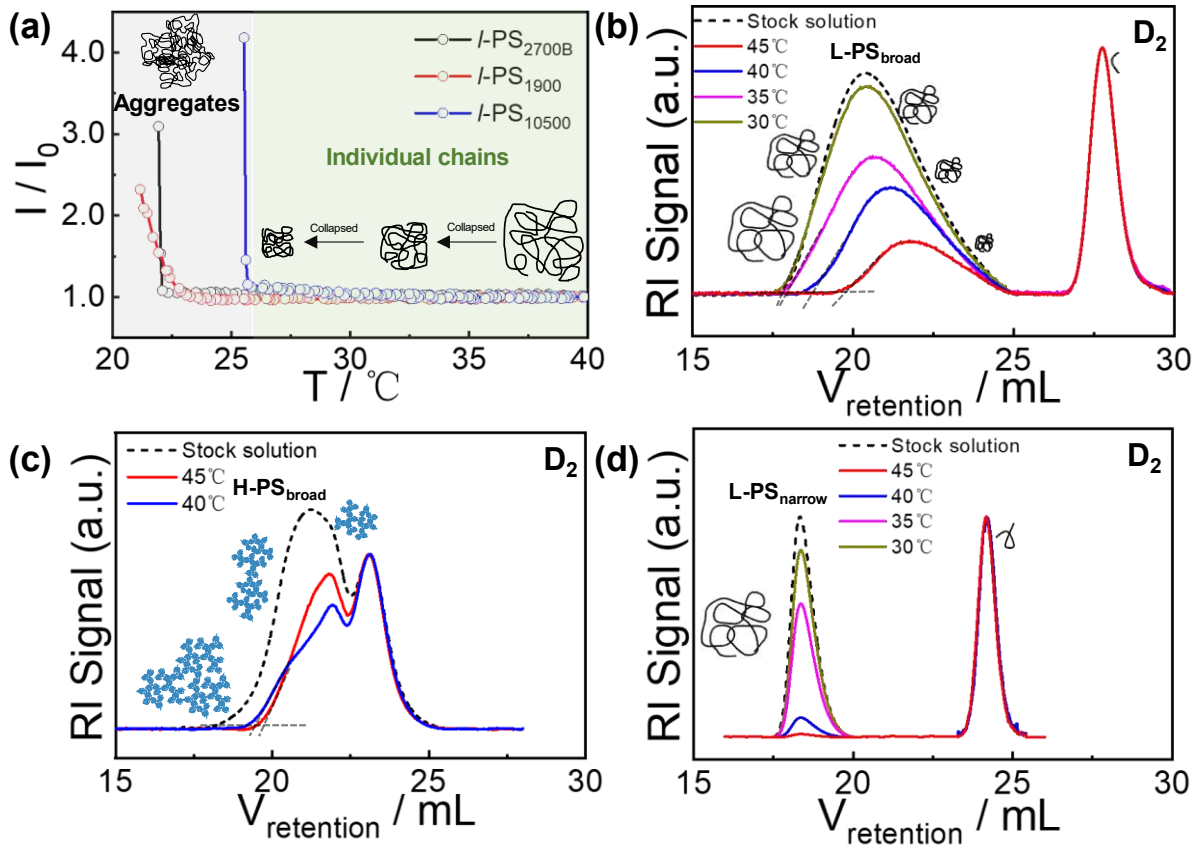


Figure 6. Temperature Dependence of Interception Behavior for Linear and Hyperbranched Polystyrene. (a) Static light scattering measurements of temperature-dependent relative scattering intensity for linear polystyrenes in cyclohexane. (b) Temperature-dependent interception profiles of broadly dispersed linear PS in cyclohexane. (c) Temperature-dependent interception profiles of broadly dispersed hyperbranched PS in cyclohexane. (d) Temperature-dependent interception profiles of narrowly dispersed linear PS in cyclohexane. All measured using a membrane with pore diameter D_2.

Temperature Dependence of Interception Behavior: Hyperbranched vs. Linear. The transport and interception of biopolymers such as starch and glycogen in porous media are often

influenced by changes in external conditions. Therefore, we further examined whether the interception behavior of branched and linear polymers exhibits significant temperature dependence. Cyclohexane, a typical theta solvent for PS, was selected because PS chains display pronounced temperature-dependent conformational changes in this solvent. Near the theta temperature (T_θ = 34.5 °C), the excluded volume parameter *v* changes sign, allowing us to decouple topological effects from solvent-mediated interactions. Below T_θ, chains collapse and excluded volume is negative; above T_θ, chains swell with positive excluded volume. This solvent system thus provides a sensitive means to assess whether interception is governed primarily by chain size (temperature-dependent) or by branching topology (temperature-invariant).

First, static light scattering was used to measure the temperature dependence of scattering intensity (**Figure 6a**). For both narrowly distributed (L-PS_{1900}, L-PS_{10050}) and broadly distributed (L-PS_{2700B}) samples, significant intermolecular aggregation was observed in the 20-30 °C range, reflected by a decrease in scattering intensity with decreasing temperature. Above T = 30 °C, the chains remained well-dispersed in a collapsed single-chain state. **Figures 6b-c** further illustrate the distinct temperature dependence of interception between linear and hyperbranched chains. Ultra-low molecular weight components were included as internal standards for concentration correction. Specifically, for linear chains at two characteristic temperatures (T = 35 °C and 40 °C), the critical interception size shifted from $R_{h,c} \approx 35$ nm to 55 nm. In contrast, for branched systems, the corresponding sizes remained nearly constant at approximately 20 nm and 23 nm.

It is important to emphasize that lowering the temperature introduces two competing effects: reduced conformational dimensions, which favor diffusion, and enhanced intrachain excluded

volume, which promotes molecular interception. In branched systems, experimental results clearly indicate that the latter dominates. Control experiments consistently demonstrate that branching topology is the key factor governing the interplay between conformational size and excluded volume. These findings imply that for weakly branched or linear polymers, interception can be effectively tuned by temperature via conformational modulation. As shown in **Figure 6d**, a narrow temperature window can shift linear chains from nearly complete interception to nearly complete translocation. This phenomenon provides a robust basis for developing novel separation and characterization strategies—for instance, enabling temperature-regulated transport and interception of components with similar sizes but different chemical compositions or branching architectures by exploiting differences in their conformational temperature dependence.

The pronounced temperature dependence of linear chains—contrasted with the near-invariance of hyperbranched chains—strongly suggests that interception in the weak-compression limit is governed not merely by chain dimensions, but by topology-modulated conformational fluctuations and excluded volume interactions. To directly probe these molecular-scale features, we turn to all-atom molecular dynamics simulations.

Conformational Distribution and Fluctuation by Computational Simulations. The experimentally observedscaling suggests that branching not only reduces chain dimensions but also alters the free-energy landscape for pore entry. To elucidate the molecular origin of topology-dependent conformational properties, we performed all-atom molecular dynamics simulations on polymer systems with distinct architectures—linear, comb-like, hyperbranched, and dendritic—each comprising 700 monomer units. **Figure 7a** schematically outlines these molecular architectures, setting the structural foundation for comparative analysis. Although

hyperbranched polymers are conceptually positioned to exhibit conformational fluctuations intermediate between flexible linear chains and rigid, non-fluctuating hard spheres, the precise quantitative role of branching topology in modulating these dynamics remained unresolved.

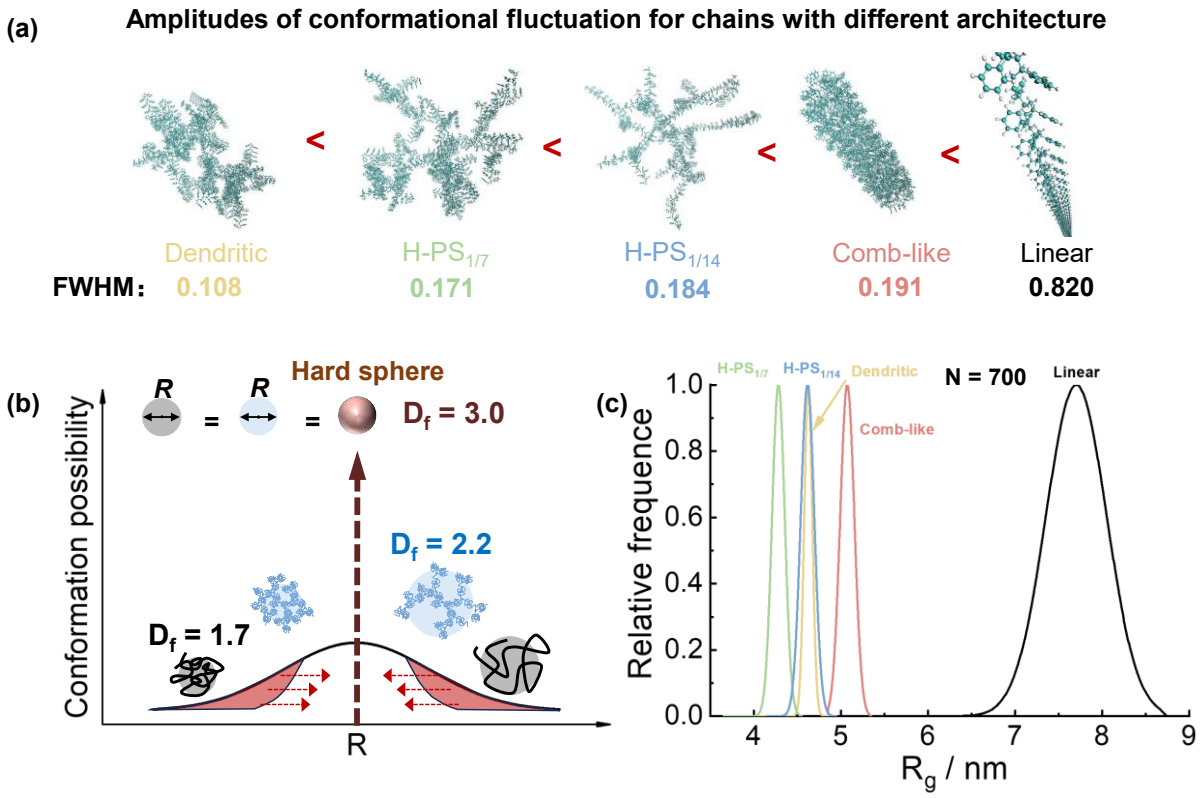


Figure 7. Conformational Distribution and Fluctuation Amplitude of Polymers with Different Topologies. (a) Ranking of conformational fluctuation amplitudes for linear, comb-like, hyperbranched, and dendritic chains from all-atom MD simulations. (b) Schematic comparison from linear chains to hyperbranched polymers and solid hard spheres. (c) Relative frequency versus radius of gyration for linear, comb-like, hyperbranched, and dendritic chains from all-atom MD simulations.

Accordingly, the simulations targeted four interrelated aspects inaccessible to direct experiment: (1) equilibrium size distributions and shape anisotropy across topologies; (2) time-dependent dimensional fluctuations and their correlation with branch length; (3) spatial monomer density profiles and their influence on effective excluded volume; and (4) the interplay among chain configuration, branch density, and rigidity under confinement-mimicking conditions. Hyperbranched variants were explicitly designed with two branch densities—approximately 7 and 14 monomers per branch—to isolate architectural effects.

The conformational landscape reveals a clear architectural progression. Quantified by the full width at half maximum (FWHM) of the radius-of-gyration distribution—a direct indicator of conformational heterogeneity and fluctuation magnitude—the data in **Figure 7b** establish a consistent hierarchy: dendritic (0.108) < hyperbranched (ρ = 1/7, 0.171) < hyperbranched (ρ = 1/14, 0.184) < comb-like (0.191) < linear (0.820). This ordering demonstrates that increasing branching density progressively suppresses conformational freedom. Complementing this metric, **Figure 7c** presents the normalized radius-of-gyration distributions, where the sharply peaked profiles of dendritic and hyperbranched chains visually affirm their restricted conformational ensembles relative to the broad, heterogeneous distributions of linear and comb-like architectures.

These computational insights provide a molecular rationale for experimental findings: the constrained conformational dynamics inherent to branched topologies directly account for their compact solution structures and reduced critical interception sizes under nanoconfinement. By explicitly linking branching architecture to fluctuation amplitude, spatial crowding, and configurational stability, the simulations establish a mechanistic framework that bridges molecular topology with emergent transport behavior in confined environments.

Theoretical Analysis Based on Flory Argument and Blob Picture. Based on the experimentally observed power-law relationship between the critical interception size and branching density ($2R_{h,c}/D \sim \rho^{-1/2}$), we further employed a combination of Flory mean-field theory and the blob model to theoretically analyze the potential dependence of the diffusion free energy barrier on molecular topology. According to the mean-field theory for a single polymer chain[37, 38], the free energy of a polymer chain with arbitrary architecture can be expressed as:

$$A / k_B T \approx \frac{R^2}{R_0^2} + \frac{b^3}{V} N_{\text{total}}{}^2 \quad (1)$$

where the first term on the right-hand side represents the contribution of conformational entropy, and the second term represents the contribution of monomer-monomer interactions. R and R_0 denote the real and ideal chain dimensions, respectively; $V \sim R^3$ is the occupied volume of the chain; b is the monomer size, and N is the degree of polymerization. Minimizing Eq. (1) with respect to R yields the chain size in a good solvent for arbitrary topology:

$$R \sim \left(R_0^2 N_{\text{total}}{}^2 b^3 \right)^{\frac{1}{5}} \quad (2)$$

On the other hand, the ideal dimension of linear and hyperbranched chains can be expressed as:

$$R_0 \sim N_{\text{total}}{}^{\frac{1}{4}} N_{\text{sub}}{}^{\frac{1}{4}} b \quad (3)$$

where N_{total} and N_{sub} are the degrees of polymerization for the whole chain and the branch chain, respectively, and the branching density $\rho = 1/N_{\text{sub}}$. For linear chains ($N_{\text{total}} = N_{\text{sub}}$), $\alpha = 1/2$, $\beta = 0$; for hyperbranched chains, $\alpha = 1/4$, $\beta = 1/4$. Substituting Eq. (3) into Eq. (2) gives the chain size in a good solvent:

$$R \sim N_{\text{total}}{}^{\alpha} N_{\text{sub}}{}^{\beta} b \quad (4a)$$

Specifically, for linear and hyperbranched chains, R is expressed as:

$$R \sim N_{\text{total}}{}^{\frac{3}{5}} b \qquad \text{Linear chain} \quad (4b)$$

$$R \sim N_{\text{total}}{}^{\frac{1}{2}} N_{\text{sub}}{}^{\frac{1}{10}} b \qquad \text{Hyperbranched chain} \quad (4c)$$

Similarly, when a chain is confined within a cylindrical pore of diameter D, its confined length (L) can be obtained by minimizing a modified free energy expression:

$$A / k_B T = \frac{L^2}{R_0^2} + \frac{b^3}{LD^2} N_{\text{total}}{}^2 \quad (5)$$

$$L \sim \left(\frac{R_0 b^3 N_{\text{total}}{}^2}{D^2} \right)^{\frac{1}{3}} \tag{6}$$

Combining Eqs. (4) and (6) gives the normalized confined length L and critical confined volume (V):

$$\frac{L}{D} \sim \left(\frac{R}{D} \right)^{\frac{5}{3}} \tag{7}$$

$$V = LD^2 \sim D^2 \left(\frac{R}{D} \right)^{\frac{5}{3}} \tag{8}$$

This indicates that the confinement scale primarily depends on the initial chain size and the pore diameter. Although Flory's mean field theory can accurately provide the dimensions of polymer chains before and after being restricted, the estimation of free energy deviates significantly from the true value.[37, 38] To analyze the activation energy, we use the blob model, treating the confined chain as a string of blobs of size ξ. The size of each blob satisfies:

$$\xi \sim N_\xi^{\alpha'} N_b^{\beta'} b \tag{9}$$

where N_ξ is the number of monomers per blob. According to the segment density conservation:

$$\frac{N_{\text{total}}}{V} = \frac{N_\xi}{\xi^3} \tag{10}$$

Combining Eqs. (4), (9), and (10) yields:

$$\xi \sim \left(\frac{N_{\text{total}} N_{\text{sub}}{}^{\beta'/\alpha'}}{R^{5/3} D^{4/3}} \right)^{\frac{\alpha'}{1-3\alpha'}} \sim \left[R^{\left(\frac{\alpha'}{\alpha} - \frac{5\alpha'}{3}\right)} N_{\text{sub}}{}^{\left(\beta' - \frac{\alpha'}{\alpha}\beta\right)} \right]^{\frac{1}{1-3\alpha'}} D^{-\frac{4\alpha'}{3(1-3\alpha')}} \tag{11}$$

For linear chains, assuming the chain structure and conformation within a blob remain consistent with the unperturbed state (where $N_{\text{total}} = N_{\text{sub}}$, $\alpha' = \alpha = 3/5$, and $\beta' = \beta = 0$), the blob size scales as $\xi \sim D$. In contrast, for hyperbranched chains under the same assumption ($\alpha' = \alpha = 1/2$, $\beta' = \beta = 1/10$), the blob size scales as $\xi \sim (R/D)^{-1/3}D$. This highlights a key difference: the

blob size in hyperbranched chains depends strongly on both the original chain size and pore diameter, unlike in linear chains.

Under the condition of weak compression limit, a central question is whether the energy barrier for diffusion through the pore depends solely on the initial chain size or also on the branching density. We thus analyze the normalized energy barrier $\Delta E/(k_BT)$, which is proportional to the total number of blobs in the nanoconfined space.

$$\frac{\Delta E}{k_B T} \sim \frac{N_{\text{total}}}{N_{\xi}} = \frac{LD^2}{\xi^3} \tag{12}$$

Using Eqs. (7) and (11), and noting that $N_{sub} \sim \rho^{-1}$, we derive:

$$\frac{\Delta E}{k_B T} \sim \frac{1}{\xi^3} \sim N_{\text{sub}}^{\frac{3}{3\alpha'-1}(\frac{\alpha\beta'-\alpha'\beta}{\alpha})} \tag{13}$$

In Eq. (13), the sign of the exponent $(\alpha\beta' - \alpha'\beta)$ is critical. For hyperbranched chains in the free state, $\alpha = 1/2$ and $\beta = 1/10$. Under weak confinement at interception boundary, chain segment density more or less increases, leading to $\alpha' < \alpha$ and $\beta' < \beta$, with $\alpha' + \beta' < 3/5$. For example, in the strong confinement limit (hard-sphere regime), $\alpha' = 1/3$ and $\beta' = 0$ result in $(\alpha\beta' - \alpha'\beta) = -1/30$. This negative exponent confirms that ΔE slightly decreases with N_{sub}. Considering that $\rho = 1/N_{sub}$, ΔE actually slightly increases with the branching density ρ. Simple numerical analysis across plausible values (e.g., α' ranging from 1/3 to 1/2, β' from 0 to 1/10) consistently yields $(\alpha\beta' - \alpha'\beta) < 0$, supporting the generality of this trend.

This theoretical framework qualitatively supports the experimental observation: higher branching density introduces a slightly higher free energy barrier for chain diffusion through nanochannel. Thus, the $\rho^{-1/2}$ scaling in interception size arises not only from compact chain architectures but also from topology-dependent energy barriers, providing a mechanistic foundation for the observed phenomena.

1

Conclusion

This study systematically investigated the nanoscale transport behavior of polymers with varying topological architectures through an integrated approach combining precisely synthesized hyperbranched polystyrene (H-PS) samples, well-defined anodic aluminum oxide (AAO) nanopores, all-atom molecular dynamics simulations, and theoretical scaling analysis. By decoupling the effects of branching density, pore geometry, and flow conditions, we established a comprehensive structure–transport relationship under weak compression limits. Key findings reveal that: (1) The critical interception size ($R_{h,c}$) exhibits a distinct power-law dependence on branching density (ρ), roughly described by the scaling of $R_{h,c} \sim \rho^{-1/2}$, which is significantly smaller than that of linear chains across pore diameters ranging from 28 to 96 nm. (2) While temperature variation noticeably alters the dimensions of linear chains and their interception behavior, $R_{h,c}$ remains nearly constant for hyperbranched architectures, underscoring that topology—rather than solvent-mediated excluded volume effects—dominates the interception process in the weak-flow regime. (3) A combined theoretical and simulation analyses demonstrate that the free energy barrier for pore translocation is strongly topology-dependent, with hyperbranched chains facing a higher entropic barrier due to restricted conformational fluctuations;

The underlying physical origin of these observations can be mainly attributed to two interrelated mechanisms: the topology-dependent free energy barrier and the conformational distribution breadth. Hyperbranched chains, with their compact and rigid architectures, undergo limited conformational fluctuations, leading to a narrowed distribution curve and a higher energy barrier for pore entry. In contrast, linear chains possess broad conformational distributions, enabling a finite probability of transiently contracting to a smaller size and thereby

broadening the effective interception size. These two mechanisms are intrinsically linked—the confined fluctuations of hyperbranched chains directly raise the initial free energy barrier for translocation.

This work not only resolves long-standing questions regarding the role of branching topology in nanopore transport but also establishes a unified physical framework for understanding polymer translocation across biological and synthetic systems. The insight that molecular architecture can be leveraged to tune transport selectivity offers promising avenues for the design of advanced separation membranes, nanofiltration systems, and biomimetic channels. Future studies extending these principles to dynamic conditions, polydisperse systems, and heterogeneous pore networks could further unlock the potential of topology-engineered polymers in nanoscale fluidic applications.

Acknowledgment. The National Natural Science Foundation of China (22322303), the Natural Science Foundation for Distinguished Young Scholars of Guangdong Province (2023B1515020001), and the Shenzhen Government's Plan of Science and Technology (RCYX20210706092101012) are gratefully acknowledged.

Reference

(1) Khan, S.; Kingston, J.; Moinuddin, Z. Renal Physiology: Blood Flow, Glomerular Filtration, and Plasma Clearance. *Anaesth. Intensiv. Care Med.* **2024**, *25*, 344-347.

(2) Zhang, N.; Tang, W.; Torres, L.; Wang, X.; Ajaj, Y.; Zhu, L.; Luan, Y.; Zhou, H.; Wang, Y.; Zhang, D.; et al. Cell Surface RNAs Control Neutrophil Recruitment. *Cell* **2024**, *187*, 846-860.

(3) Ritmejeris, J.; Chen, X.; Dekker, C. Single-Molecule Protein Sequencing with Nanopores. *Nat. Rev. Bioeng.* **2025**, *3*, 303-316.

(4) Lu, C.; Bonini, A.; Viel, J. H.; Maglia, G. Toward Single-Molecule Protein Sequencing Using Nanopores. *Nat. Biotechnol.* **2025**, *43*, 312-322.

(5) Javidanbardan, A.; Messerian, K. O.; Zydney, A. L. Membrane Technology for the Purification of RNA and DNA Therapeutics. *Trends Biotechnol.* **2024**, *42*, 714-727.

(6) Liang, J.; Huang, Q.; Wu, L.; Shi, X.; Yan, K.; Guo, F.; Zhou, Z.; Li, G. A GOX/RGO-CS-Fc/AuNPs Nanosensing Membrane in a Light-Addressable Potentiometric Biosensor for Glucose Specific Detection. *Microchem J.* **2024**, *200*, 110478.

(7) Gao, W.; Wang, Z.; Duan, F.; Li, Y.; Shi, S.; Sun, Z.; Zhou, B.; Lv, L. Comprehensive Assessment of Membrane Technology for Typical Water Treatment Processes: A Critical Review. *Desalination* **2025**, *614*, 119171.

(8) de Gennes, P. G. Coil‐Stretch Transition of Dilute Flexible Polymers under Ultrahigh Velocity Gradients. *J. Chem. Phys.* **1974**, *60*, 5030-5042.

(9) Freed, K. F.; Wu, C. General Approach to Polymer Chains Confined by Interacting Boundaries. II. Flow through a Cylindrical Nano-Tube. *J. Chem. Phys.* **2011**, *135*, 144902.

(10) de Gennes, P. G. *Scaling Concepts in Polymer Physics*; Cornell University Press, 1979.

(11) de Gennes, P. G. Flexible Polymers in Nanopores. *Adv. Polym. Sci* **1999**, *138*, 91-105.

(12) Brochard, F.; de Gennes, P. G. Dynamics of Confined Polymer Chains. *J. Chem. Phys.* **1977**, *67*, 52-56.

(13) Ding, M.; Duan, X.; Shi, T. Polymer Escape from Confining Nanotube in Reverse Flow. *Macromolecules* **2017**, *50* , 7777-7782.

(14) Wang, Z.; Wang, R.; Lu, Y.; An, L.; Shi, A.-C.; Wang, Z.-G. Mechanisms of Flow-Induced Polymer Translocation. *Macromolecules* **2022**, *55*, 3602-3612.

(15) Adamski, R. P.; Anderson, J. L. Configureurational Effects on Polystyrene Rejection from Microporous Membranes. *J. Polym. Sci. Pt. B-Polym. Phys.* **1987**, *25*, 765-775.

(16) Ge, H.; Pispas, S.; Wu, C. How Does a Star Chain (Nanooctopus) Crawl through a Nanopore? *Polym. Chem.* **2011**, *2*, 1071-1076。

(17) Li, L.; He, C.; He, W.; Wu, C. How Does a Hyperbranched Chain Pass through a Nanopore? *Macromolecules* **2012**, *45*, 7583-7589.

(18) Hendrickson, G. R.; Lyon, L. A. Microgel Translocation through Pores under Confinement. *Angew. Chem.-Int. Edit.* **2010**, *49*, 2193-2197.

(19) Zheng, T.; Yang, J.; He, J.; Li, L. Origin of Inconsistency in Experimentally Observed Transition Widths and Critical Flow Rates in Ultrafiltration Studies of Flexible Linear Chains. *Macromolecules* **2018**, *51*, 6504-6512.

(20) Jin, F.; Wu, C. Observation of the First-Order Transition in Ultrafiltration of Flexible Linear Polymer Chains. *Phys. Rev. Lett.* **2006**, *96*, 237801.

(21) Hwang, J.; Kokini, J. L. Structure and Rheological Function of Side Branches of Carbohydrate Polymers. *J. Texture Stud.* **1991**, *22*, 123-167.

(22) Ding, M.; Li, L. Flow-Induced Translocation and Conformational Transition of Polymer Chains through Nanochannels: Recent Advances and Future Perspectives. *Macromolecules* **2021**, *54*, 9773-9793.

(23) Lu, L.; Wang, Z.; Shi, A.; Lu, Y.; An, L. Polymer Translocation. *Chin. J. Polym. Sci.* **2023**, *41*, 683-698.

(24) Wang, Z.; Wang, Z.; Shi, A.; Lu, Y.; An, L. Behaviors of a Polymer Chain in Channels: From Zimm to Rouse Dynamics. *Macromolecules* **2023**, *56*, 2447-2453.

(25) Li, L.; Lu, Y.; An, L.; Wu, C. Experimental and Theoretical Studies of Scaling of Sizes and Intrinsic Viscosity of Hyperbranched Chains in Good Solvents. *J. Chem. Phys.* **2013**, *138*, 114908.

(26) Lu, Y.; An, L.; Wang, Z. Intrinsic Viscosity of Polymers: General Theory Based on a Partially Permeable Sphere Model. *Macromolecules* **2013**, *46*, 5731-5740.

(27) Patten, T. E.; Xia, J. H.; Abernathy, T.; Matyjaszewski, K. Polymers with Very Low Polydispersities from Atom Transfer Radical Polymerization. *Science* **1996**, *272*, 866-868.

(28) Jakubowski, W.; Matyjaszewski, K. Activators Regenerated by Electron Transfer for Atom-Transfer Radical Polymerization of (Meth)acrylates and Related Block Copolymers. *Angew. Chem.-Int. Edit.* **2006**, *45*, 4482-4486.

(29) Kong, L.; Sun, M.; Qiao, H.; Pan, C. Synthesis and Characterization of Hyperbranched Polystyrene via Click Reaction of AB_2 Macromonomer. *J. Polym. Sci. Pol. Chem.* **2010**, *48*, 454-462.

(30) Rharbi, Y.; Zhang, J.; Spiro, J. G.; Chen, L.; Winnik, M. A.; Vavasour, J. D.; Whitmore, M. D.; Jérôme, R. An Energy Transfer Study of Homopolymer Localization in Block Copolymers. *Macromolecules* **2003**, *36*,

1241-1252.

(31) Sapir, L.; Chen, D.; Rubinstein, M. Reduction of Kuhn Length upon Chain Extension. *ACS Macro Lett.* **2025**, *14*, 1827-1834.

(32) Fisch, M.; Primak, A.; Kumar, S. X-ray Diffraction Study of Anodisc Filters. *Phys. Rev. E*. **2002**, *65*, 046615.

(33) Béguin, L.; Grassl, B.; Brochard-Wyart, F.; Rakib, M.; Duval, H. Suction of Hydrosoluble Polymers into Nanopores. *Soft Matter* **2011**, *7*, 96-103.

(34) Zheng, T.; Zhu, M.; Yang, J.; He, J.; Waqas, M.; Li, L. Revisiting the Flow-Driven Translocation of Flexible Linear Chains through Cylindrical Nanopores: Is the Critical Flow Rate Really Independent of the Chain Length? *Macromolecules* **2018**, *51*, 9333-9343.

(35) Masuda, H.; Fukuda, K. Ordered Metal Nanohole Arrays Made by a Two-Step Replication of Honeycomb Structures of Anodic Alumina. *Science* **1995**, *268*, 1466-1468.

(36) Han, H.; Park, S.; Jang, J.; Ryu, H.; Kim, K.; Baik, S.; Lee, W. In Situ Determination of the Pore Opening Point during Wet-Chemical Etching of the Barrier Layer of Porous Anodic Aluminum Oxide: Nonuniform Impurity Distribution in Anodic Oxide. *ACS Appl. Mater. Interfaces* **2013**, *5*, 3441-3448.

(37) Michael Rubinstein, R. H. C. *Polymer Physics*; Oxford University Press, 2003.

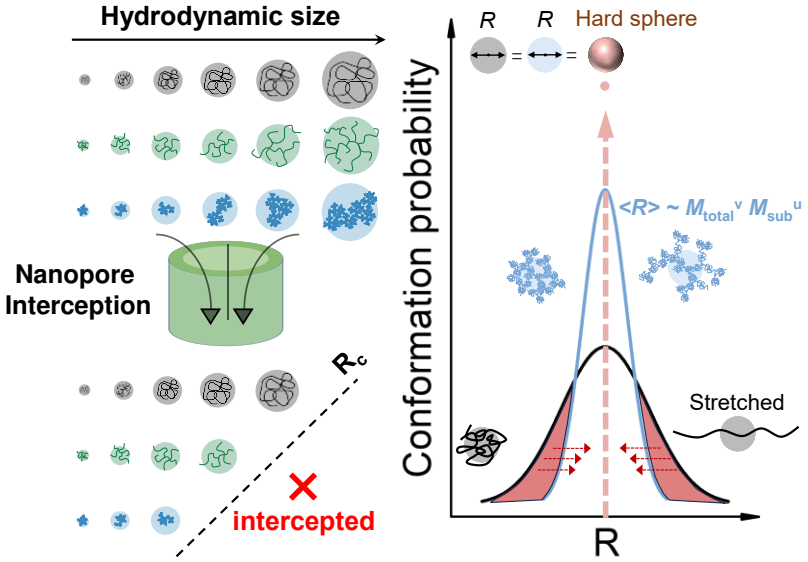
(38) Teraoka, I. *Polymer solutions: An Introduction to Physical Properties*; John Wiley & Sons, 2002.

For Table of Contents Use Only

Conformational Entropy Bottleneck Underlies Nanopore Interception of Polymers: Dominant Roles of Branching Architecture and Excluded Volume

by

Yiren Wang, Haorong Huang, Jiawen Yang, Xin Guan, Mo Zhu, Mingming Ding, Lianwei Li*



Supplementary Files

This is a list of supplementary files associated with this preprint. Click to download.

- SupplementaryInformation20260206.docx